CrystEngComm

PAPER

View Article Online
View Journal | View Issue

Cite this: *CrystEngComm*, 2015, **17**, 6962

Matching the organic and inorganic counterparts during nucleation and growth of copper-based nanoparticles – *in situ* spectroscopic studies†

Malwina Staniuk,[a] Daniel Zindel,[b] Wouter van Beek,[c] Ofer Hirsch,[a] Niklaus Kränzlin,[a] Markus Niederberger[a] and Dorota Koziej*[a]

Received 4th March 2015,
Accepted 26th May 2015

DOI: 10.1039/c5ce00454c

www.rsc.org/crystengcomm

Although syntheses in organic solvents provide access to a wide range of copper-based nanoparticles, the correlation between organic reactions in solution and nucleation and growth of nanoparticles with defined properties is not well understood. Here, we utilize the Multivariate Curve Resolution-Alternative Least Squares (MCR-ALS) methodology to examine spectroscopic data recorded *in situ* during the synthesis of copper-based nanoparticles. While earlier studies showed that depending on the temperature copper(II) acetylacetonate reacts with benzyl alcohol and forms either copper oxides or copper nanoparticles, we link the inorganic reaction with their organic counterparts. From X-ray Absorption Near Edge Spectroscopy (XANES) and Ultraviolet-visible spectroscopy (UV-vis) data we learn that copper(I) oxide forms directly from the solution and is the final product at low temperature of 140 °C. We observe in Fourier Transformed Infrared (FTIR) spectra an increasing concentration of benzyl acetate that co-occurs with the formation of a copper enolate and evolution of benzaldehyde, which accompanies the reduction of copper ions. We also record the interaction of organic species at the Cu_2O surface, which inhibits a further reduction to metallic copper. When we raise the synthesis temperature to 170 °C it turns out that the Cu_2O is just an intermediate species. It subsequently transforms by solid-state reduction to metallic copper accompanied by oxidation of benzyl alcohol to benzaldehyde.

1. Introduction

Twenty years after the initial findings[1] the nonaqueous sol–gel process is now an established method used to synthesize crystalline nanoparticles of customizable size, composition and functionalities.[2–6] Specially for metal oxides, the advancement has been made possible due to the understanding that solvents are not only reaction medium but may also be an oxygen source and act as stabilizing agent. That knowledge has been gained by studying the organic compounds forming during synthesis.[7–13] When benzyl alcohol is used as a solvent, the most common routes are: alkyl halide elimination, ester elimination, ether elimination, aldol condensation and C–C bond formation between benzylic alcohols and alkoxides.[5,12,14–16] Remarkably, for some metal oxides with the occurrence of nanoparticles, the organic reactions do not terminate, and in fact, new reactions are initiated.[17–21] By far the most intriguing example is the formation of monolithic tungsten oxide-polybenzylene hybrids induced by the nucleation of tungsten oxide nanoparticles and their catalytic activity.[20] Moreover, in the last decade, the non-aqueous method has been further adopted to synthesize metal phosphates, -sulfides, -diimides and even metallic nanoparticles.[18,22–25] With the increased complexity of the inorganic product also the linkage of the inorganic species to their respective organic counterparts became more challenging.

Here, our main focus is the determination of organic and inorganic species formed during the nucleation and growth of copper-based nanoparticles and their interdependence by utilizing different spectroscopic techniques. The latest development of synchrotron- and laboratory-based equipment and analysis tools allow for *in situ* monitoring the complex reactions in solution.[7,26–36] However, the specificity of the individual methods often makes a quantitative analysis or a direct comparison of results difficult. We overcome this problem by selecting two spectroscopic methods, X-ray Absorption Near Edge Spectroscopy (XANES) and Ultraviolet–visible spectroscopy (UV-vis), which even though they probe fundamentally different phenomena,

[a] *Laboratory for Multifunctional Materials, Department of Materials, ETH Zurich, Vladimir-Prelog-Weg 5, 8093 Zurich, Switzerland.*
E-mail: dorota.koziej@mat.ethz.ch
[b] *Laboratory of Physical Chemistry, ETH Zurich, Vladimir-Prelog-Weg 2, 8093 Zurich, Switzerland*
[c] *Swiss-Norwegian Beamlines at European Synchrotron Research Facility, 71 Avenue des Martyrs, 38043 Grenoble, France*

† Electronic supplementary information (ESI) available: See DOI: 10.1039/c5ce00454c

provide information on the chemical composition. In order to determine the changes of the composition of the reaction solution during nucleation and growth of Cu_2O and Cu nanoparticles we apply Multivariate Curve Resolution-Alternative Least Squares (MCR-ALS) method. It has been previously successfully used to determine the concentration profile and pure XANES spectra of individual species during *in situ* studies of Cu-catalysts, Cu-doped V_2O_3 batteries and to follow the synthesis of Co, TiO_2 and Ni-doped MoO_2 nanoparticles.[18,37–45]

Additionally, we track the formation of organic compounds by Fourier Transform Infrared spectroscopy (FTIR) studies that are recorded simultaneously with UV-vis measurements. In the control experiments without copper precursor, we: (a) evaluate the decomposition of benzyl alcohol upon heating, (b) determine the lower detection limit and (c) calibrate the curve for benzaldehyde, benzyl acetate and dibenzyl ether, compounds that are considered the main organic counterparts of copper-based nanoparticle nucleation. This lays the foundation for a quantitative analysis of *in situ* FTIR studies. We find that only the formation of benzyl acetate correlates directly with the occurrence of copper-based nanoparticles in benzyl alcohol. At low reaction temperature, the formation of benzaldehyde as a product of Cu_2O synthesis makes up approximately thirty percent of the total amount of benzaldehyde. The remaining seventy percent are a product of catalytic activity of Cu_2O nanoparticles. At high reaction temperature, Cu_2O nanoparticles are further reduced to Cu. Interestingly, the formation of copper nanoparticles terminates the catalytic formation of benzaldehyde, and instead triggers the catalytic formation of dibenzyl ether.

2. Experimental

Chemicals

Benzyl alcohol (99–100.5%,), benzaldehyde (≥99%), dibenzyl ether (99%), and copper hydroxide ($Cu(OH)_2$) (technical grade) were supplied by Sigma Aldrich, copper(II) acetylacetonate (98%) by Acros Organics, benzyl acetate (99%), ethanol (99.8%) by Fluka and tetrahydrofuran by Riedel-de-Haen (99.9%, stabilized by butylhydroxytoluol (BHT)). The chemicals were used without any further purification. CuO was obtained by thermal oxidation of Cu_2O.[46]

Synthesis procedure

Synthesis at the synchrotron. $Cu(acac)_2$ (1 mmol) was added to 20 mL of benzyl alcohol. Then 1 mL of the reaction mixture was transferred to a reactor with a total volume of 1.66 mL.[18] The solution was heated to 180 °C and kept for 343 minutes. The reaction reached 180 °C after around 3–4 minutes.

Synthesis in the laboratory. The synthesis was performed in a Mettler Toledo EasyMax Synthesis Workstation. 60 mL of benzyl alcohol were heated to 140 or 170 °C in a 100 mL reactor. $Cu(acac)_2$ (4.2 mmol) was added to the preheated benzyl alcohol and kept for 4050 minutes (140 °C) or 326 minutes (170 °C). The precipitate was centrifuged and washed three times with ethanol.

Ex situ characterization

X-ray Absorption Spectroscopy (XAS) data of the corresponding powder pellets were measured at the Swiss Norwegian Beamline (SNBL) BM01B at the European Synchrotron Research Facility (ESRF) from 8.850 to 9.800 keV in continuous scanning mode with two ion chambers, one before the sample and one after the sample. The powders were diluted in cellulose to optimize the edge-step and pressed into pellets. Powder X-ray diffraction (PXRD) patterns of synthesized powders were collected on an Empyrean powder diffractometer (PANalytical B.V., The Netherlands), operating in reflection mode under constant irradiated area conditions with Cu Kα radiation (45 kV, 40 mA). Scanning electron microscopy (SEM) images were taken on a Magellan 400 FEG (FEI, USA) to show the shape and morphology of the nanoparticles. Gas chromatography-mass spectrometry (GC-MS) analysis of the filtered reaction liquids was performed with a Thermo Scientific Trace 1300 (GC) coupled with an ISQ single quad (MS). The samples were diluted in tetrahydrofuran (ratio 1 : 20). Attenuated total reflection (ATR)-FTIR spectra of organic samples in preheated benzyl alcohol were measured as references on a ReactIR15 (Mettler Toledo AutoChem) with a 6.5 mm AgX DiComp Fiber Conduit probe. 60 mL of benzyl alcohol were heated to 140 or 170 °C and then the corresponding organic species were added. The analyzed range was 800 to 1800 cm^{-1} and the resolution was 4 cm^{-1}.

In situ characterization

XAS. The measurements were recorded with a Vortex EM fluorescence detector equipped with Xia digital electronics. The Cu K-edge XANES spectra were recorded in the range between 8.949 to 9.049 keV with a resolution of 0.5 eV. We averaged three consecutive spectra in ATHENA software to increase signal to noise ratio.[47]

ATR-FTIR. ReactIR15 with a 6.5 mm AgX DiComp Fiber Conduit probe was used for *in situ* ATR-FTIR measurements. The spectrum of preheated benzyl alcohol was used as background. The spectra were recorded every 2 minutes for the synthesis at 140 °C and every 15 seconds for the synthesis at 170 °C. Due to deposition of particles on the probe, the measurements were paused to clean the probe: (a) at 140 °C, only in the time period between 2996 and 3067 minutes; (b) at 170 °C, starting after 30 minutes of the reaction and then every 15 minutes.

Control experiment. The decomposition of pure benzyl alcohol upon heating was measured every 5 minutes (140 °C) or every 15 seconds (170 °C). To mimic the conditions during the synthesis at 170 °C, the reactor was opened every 15 minutes. The final products were additionally investigated by GC-MS.

ATR-UV-vis. The spectra were recorded by a Cary 60 spectrophotometer (Agilent Technology) with ATR-probe with

sapphire crystal (Hellma). Spectra in the range from 800 to 300 nm were recorded every 30 seconds (140 °C) or every 36 seconds (170 °C). At 140 °C after around 7.5 hours a film of particles grew on the ATR crystal and almost fully blocked the light. In the case of synthesis at 170 °C, after 29 minutes the probe was taken out of the solution, cleaned and placed back into the reaction solution. The measurement was continued after 40 minutes.

Data handling

Extended X-ray Absorption Fine Structure (EXAFS). We performed the EXAFS data reduction using the ATHENA software. The normalization parameters (pre-edge ranges, post-edge ranges and E_0) are given in ESI† Table S1. The resulting $\chi(k)$-function was k^3 weighted and Fourier transformed (FT) using a Hanning window function.

ATR-FTIR data. We applied a baseline offset correction and shifted the *in situ* spectra so that the absorbance value was always 0 at 1800 cm^{-1}. In addition, due to the particle deposition, we divided the analyzed spectra into two sets. At 140 °C the first and second sets contained spectra before and after particle deposition on the probe, respectively. For more information please refer to ESI† Fig. S1. At 170 °C the first and second sets contained spectra recorded before and after the cleaning of the probe, respectively.

Multivariate Curve Resolution-Alternative Least Squares (MCR-ALS). *In situ* ATR-FTIR and XANES data were analyzed with the MCR-ALS, implemented under MATLAB environment and discussed by De Juan and Tauler.[37,48] The underlying idea behind MCR-ALS is the recovery of spectral components and their correlated fraction profiles from time evolving data by bilinear decomposition of experimental data, represented by matrix **D**, according to eqn (1):

$$\mathbf{D} = \mathbf{C}\mathbf{S}^{\mathbf{T}} + \mathbf{E} \quad (1)$$

Rows of matrix **D** are spectra acquired during measurement, columns of matrix **C** and rows in matrix $\mathbf{S}^{\mathbf{T}}$ are concentration profiles and spectra of resolved components, respectively. Matrix **E** contains residuals not explained by the model. Eqn (1), generally valid for spectroscopic data governed by the Lambert–Beer law like XANES or FTIR, is solved by ALS algorithm, which iteratively calculates the **C** and $\mathbf{S}^{\mathbf{T}}$ matrices that fits best the experimental data. The optimization of **C** and $\mathbf{S}^{\mathbf{T}}$ is carried out for a proposed number of components. Initial estimates of **C** and $\mathbf{S}^{\mathbf{T}}$ are obtained by using SIMPLe-to-use Interactive Self-Modeling Algorithm (SIMPLISMA), which finds the most different spectra within the dataset that are further used as an input for ALS optimization.

The number of components was selected on the basis of Singular Value Decomposition (SVD). The initial spectra of the components were estimated with the PURE algorithm with the noise level set to 3% (XANES) and 4% (ATR-FTIR). Constraints applied for ALS calculation were as follows: non-negativity of spectra and concentration (XANES), non-negativity of concentration (XANES and ATR-FTIR), unimodality of concentration (XANES and ATR-FTIR), convergence criterion: 0.1 (XAS and ATR-FTIR). For more information please refer to ESI† Fig. S2–S4, Tables S2–S5.

3. Results and discussion

3.1. Synthesis

In a previous study we found that the reaction between copper(II) acetylacetonate and benzyl alcohol resulted in the formation of a metallic copper foil with Cu_2O nanoparticles as intermediates.[25] Now we adopt this synthesis to a reactor equipped with *in situ* ATR-UV-vis and -FTIR probes to collect information about the formation mechanism. In order to be able to probe the organic species in solution we prevent formation of the Cu foil at the surface of ATR crystals by vigorous stirring. Similar to the previous report at low reaction temperature cuprous oxide and at high temperature metallic copper are formed, respectively.[25] Obviously, the time required for the reduction of cuprous oxide to copper varies because of the differences in reactor volume, stirring velocity and heating rate. Therefore, for the *in situ* studies we choose temperature conditions at which the product in the Mettler Toledo reactor is phase pure. At 140 °C and 170 °C we obtain Cu_2O or Cu nanoparticles, respectively. The corresponding PXRD patterns and SEM images are shown in Fig. 1.

3.2. *In situ* studies of inorganic species in solution

(a) *In situ* XANES studies. To elucidate the mechanism of the reduction of $Cu(acac)_2$ to Cu, we measure *in situ* X-ray absorption at the Cu-K edge and analyze the oxidation state of Cu and the short-range ordering around the Cu ions as shown in Fig. 2–4. In general Cu^0, Cu^+, and Cu^{2+} exhibit the absorption edge at 8.979, 8.981 and 8.984 keV, respectively.[49–51] During synthesis we observe shifting of the absorption edge from 8.984 to 8.979 keV, which indicates the reduction of Cu^{2+} to Cu^0 as shown in Fig. 2a. Furthermore, we compare the *in situ* XANES spectra recorded in the reaction solution with the reference powders: copper oxides (CuO, Cu_2O), copper hydroxide ($Cu(OH)_2$), metallic copper (Cu) foil and nanoparticles, and copper(II) acetylacetonate ($Cu(acac)_2$) as shown in Fig. 2b. However, in the case of particles smaller than a few nanometers the position and relative intensities of pre-edge and post-edge features in XANES spectrum are also sensitive to their size and to the species adsorbed at their surface.[41] Here, the spectra of $Cu(acac)_2$, Cu_2O and Cu, which were recorded during *in situ* experiments vary from their bulk powder counterparts and thus the utilization of the linear combination analysis (LCA) to determine their relative concentration during synthesis is not possible. For the sake of completeness in Fig. 2c we compare the k^3 weighted Fourier Transform (FT) of the EXAFS spectra of the final product and the reference compounds. This further underlines the differences between the nanoparticles in solution and their bulk counterparts.

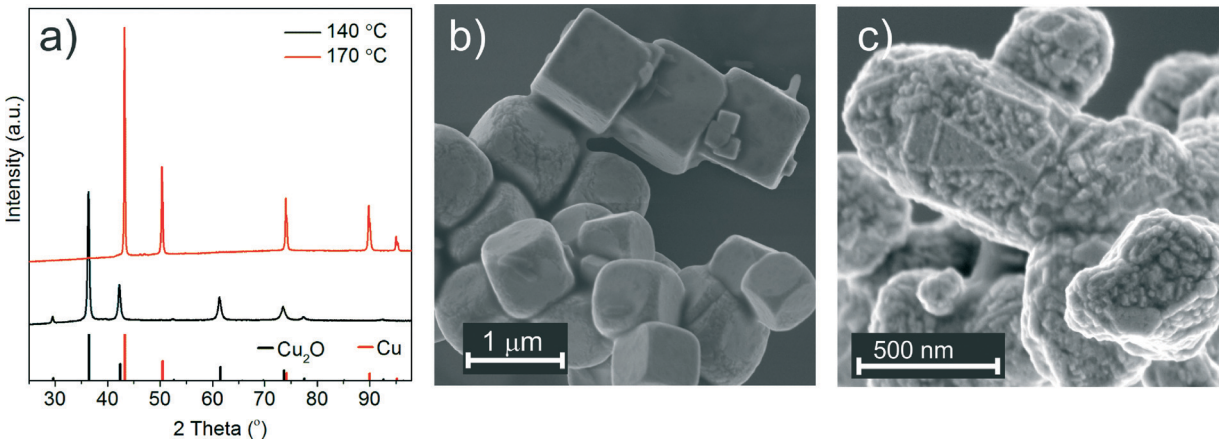

Fig. 1 (a) PXRD patterns of the nanoparticles synthesized at 140 (black pattern) and 170 °C (red pattern). Reference PXRD patterns of Cu_2O (ICDD no. 00-005-0667) and Cu (ICDD no. 01-071-4610). SEM images of (b) Cu_2O synthesized at 140 °C and (c) Cu synthesized at 170 °C.

We first determine the initial oxidation state of copper species upon dissolution in benzyl alcohol at 180 °C as shown in Fig. 3. Then, we utilize the MCR-ALS method to analyze the *in situ* XANES spectra during nucleation of copper nanoparticles. This solely variance based method allows to determine, without *a priori* knowledge, the number of components, their spectra and relative concentration in a solution as shown in Fig. 4.

Precursor. Here, a careful comparison of the XANES spectra of the precursor as pellet (red curve), dissolved in benzyl alcohol at RT (blue curve) and at 180 °C (green curve), shown in Fig. 3, reveals the subtle differences in the pre- and post-edge regions. In general, such differences are related to the changes of geometry of the first coordination sphere of the absorbing element.[52,53] Above the edge, the spectrum of solid $Cu(acac)_2$ shows more pronounced features in comparison to the $Cu(acac)_2$ in benzyl alcohol. The decrease of their intensity indicates a decrease of multiple scattering that involves second nearest neighbor or higher shells. We assign it to the loss of long-range order due to the dissolution of the precursor in benzyl alcohol. In addition, the deviation in the 1s → 4s transition indicates changes in the coordination of the copper ion, suggesting complexation with benzyl alcohol. The spectra of $Cu(acac)_2$ in benzyl alcohol at 180 °C shows, with respect to RT, an increase of the intensity of the 1s → 4p transition. We do not observe characteristic features either of the CuO or of the $Cu(OH)_2$. Thus, we can conclude that no solid CuO or the $CuOH_2$ species are formed before formation of Cu_2O.

Cu reduction at 180 °C in benzyl alcohol. To track the changes from $Cu(acac)_2$ to Cu during the reaction at 180 °C we analyze the *in situ* XANES data by MCR-ALS as shown in Fig. 4. According to SVD results, three components suffice to fit the data. We use SIMPLISMA based algorithm to find the spectra that are used as initial estimates for MCR-ALS. We show the spectra of powder references recorded at room temperature in transmission mode only as guidance, since the XANES spectra of nanoparticles strongly depend on their size, species adsorbed at their surface and temperature at which the spectrum was measured. Thus, the recovered spectra are the spectra of a given compound at the particular reaction conditions. The first recovered spectrum is the precursor dissolved in benzyl alcohol at 180 °C. The second and third spectrum show characteristic features observed in the reference spectra of Cu_2O and Cu, respectively. Therefore, the appearance of the second and third component indicates the nucleation of Cu_2O and its consecutive reduction to Cu. The concentration dependence of the three recovered components proves that Cu_2O and Cu are not formed concurrently. First, exclusively Cu_2O forms and only after 83 minutes it gets reduced to metallic copper, in line with previously reported PXRD studies.[25] The direct formation of Cu_2O confirms the reduction of Cu^{2+} to Cu^{+} in the solution and solid intermediate species like CuO and $Cu(OH)_2$ are excluded.

(b) UV-vis studies. To connect the synchrotron and the laboratory studies, we investigate the inorganic side of the reaction with UV-vis spectroscopy. Even though UV-vis and XAS spectroscopy measure different physical phenomena, the information about changes in the chemical composition that can be derived from the *in situ* studies are basically the same. This enables us to pin down the time scale of the consecutive formation of cuprous oxide and copper, and later to match them with the changes of organic species tracked with FTIR spectroscopy. Based on UV-vis spectra, shown in ESI† Fig. S5 we learn that at 140 °C the cuprous oxide nanoparticles form between 209 and 330 minutes. At 170 °C the reaction is much faster. Already after 17 minutes we observe the formation of cuprous oxide nanoparticles, followed by their consecutive growth and after 52 minutes their transformation to metallic copper nanoparticles.

3.3. Organic species forming during synthesis – complementary *in situ* ATR-FTIR and GC-MS studies

Simultaneously with UV-vis, we measure *in situ* FTIR to track the organic species forming in solution during the synthesis

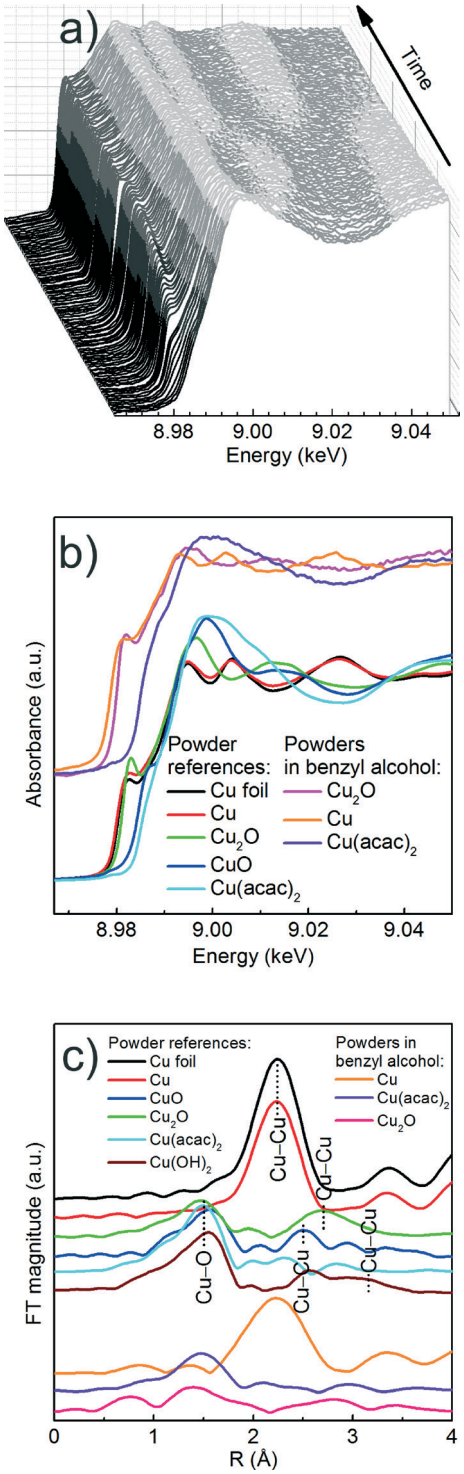

Fig. 2 Cu K-edge XAS spectra; (a) XANES spectra taken during the synthesis of copper nanoparticles from $Cu(acac)_2$ in benzyl alcohol at 180 °C; (b) comparison of XANES spectra of powder references (pellets) and powders in benzyl alcohol; Note: the spectrum of Cu_2O in benzyl alcohol was recorded at 160 °C; (c) FT EXAFS spectra of powder pellets. The spectra were shifted on the ordinate for better representation.

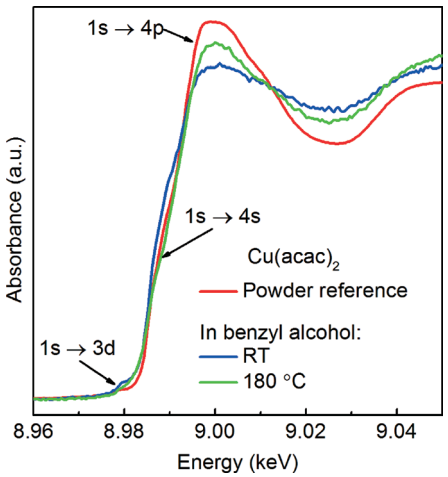

Fig. 3 Comparison of Cu K-edge XANES spectra of $Cu(acac)_2$ powder measured in transmission mode (red curve) and $Cu(acac)_2$ dissolved in benzyl alcohol at RT (blue curve) and 180 °C (green curve) measured in fluorescence mode.

of Cu-based nanoparticles at 140 and 170 °C as shown in ESI† Fig. S2a–b. In the following, we first qualitatively describe the *in situ* FTIR results. Then, the GC-MS studies give complementary information about species forming in the solution below the detection limit of FTIR. Finally, we determine the lower detection limit and calibration curve for the main organic species, which allows us to estimate their quantities and correlate the organic and the inorganic compounds.

(a) Qualitative results. Differently than for the XANES data, MCR-ALS analysis of the FTIR data does not recover the spectra of individual chemical species. Nevertheless it enables the identification of a combination of the compounds, which evolve together/at the same time or at the same rate. The MCR-ALS recovered spectra of components (Fig. S2c–d†), their concentration profiles (Fig. S3†) and the assignments of individual vibrations are given in the ESI.

At both reaction temperatures, as long as some of the precursor is present in the solution, the same organic compounds, benzyl acetate and benzaldehyde, form. At 140 °C the reaction terminates with the reduction of $Cu(acac)_2$ to Cu_2O. Only at that point the bands assigned to the species adsorbed at the surface of Cu_2O become clearly visible as shown in ESI† Fig. S4a–b. At 170 °C the nucleation of Cu_2O is only an intermediate step towards the formation of Cu nanoparticles and we do not observe adsorption of organic species at the Cu_2O surface. Instead, we observe the formation of dibenzyl ether as the product of benzyl alcohol condensation, which is a result of the catalytic activity of metallic copper.

(b) GC-MS studies. To complete our *in situ* experiments we analyze the organic compounds, which are present in benzyl alcohol after the synthesis with GC-MS. At 140 °C, in addition to benzaldehyde and benzyl acetate already observed with FTIR, we detect acetone and benzylacetone (ESI† Fig. S6a). Whereas at 170 °C, besides benzaldehyde, benzyl acetate and dibenzyl ether already observed with FTIR, we detect trace amounts of acetone and acetylacetone as shown in ESI† Fig. S6b. Moreover, we analyze the organic products of the control experiment and detect benzaldehyde

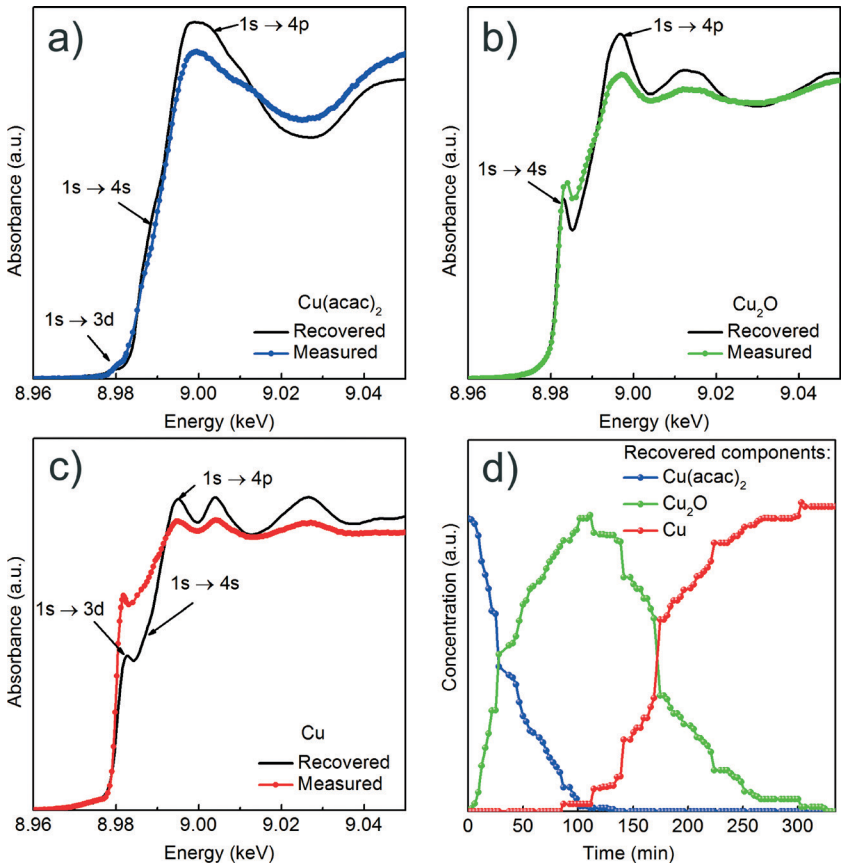

Fig. 4 Results of the MCR-ALS analysis of *in situ* Cu K-edge XANES spectra recorded in fluorescence mode; (a), (b) and (c) recovered spectra of individual components and corresponding reference spectra; The reference compounds were measured as pellets in transmission mode and are only given here as guidance; (d) concentration profiles of the three recovered components during the synthesis at 180 °C.

as well as trace amounts of dibenzyl ether and benzyl benzoate as shown in ESI† Fig. S6c–d.

In summary, comparing the organic species from these three experiments, benzyl acetate is the only compound that exclusively forms when copper-based nanoparticles crystallize. All other organic compounds may also form as products of parallel, side reactions that are not directly related to the nucleation of the copper-based nanoparticles.

(c) Towards quantitative analysis – calibration, detection limit and side reactions. Based on the *in situ* FTIR studies,

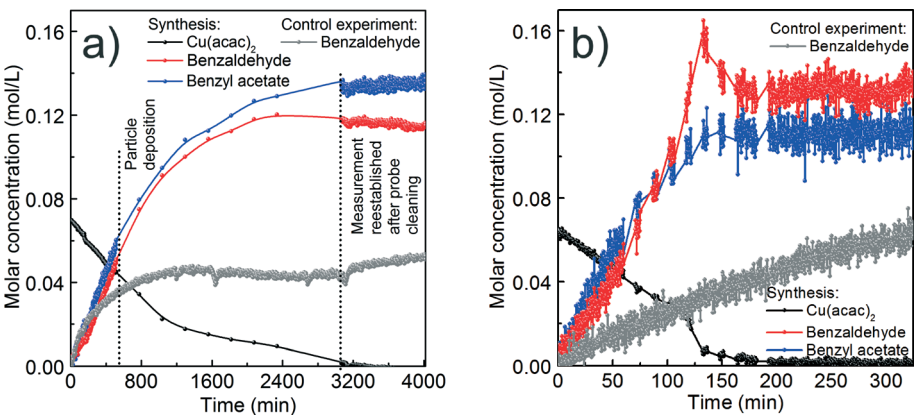

Fig. 5 Molar concentration of copper(II) acetylacetonate, benzyl acetate and benzaldehyde during the synthesis of copper-based particles as well as molar concentration of benzaldehyde from the control experiments calculated from *in situ* FTIR data; (a) reaction at 140 °C and (b) at 170 °C. We cannot fully avoid the deposition of copper oxide and copper on the surface of the ATR crystals. In a) the vertical, dashed lines indicate the start of "particle deposition" and "measurements reestablished after probe cleaning", respectively. The measurements in this time span were background-corrected.

we identify benzaldehyde, benzyl acetate and dibenzyl ether as the three main organic compounds which are formed from benzyl alcohol during crystallization of the Cu-based nanoparticles. Although, as mentioned before, not all three compounds are necessarily related to Cu formation. Their lower detection limits, when measured in heated benzyl alcohol, were determined to be 0.003, 0.007 and 0.008 M, respectively. The calibration curves are shown in ESI† Fig. S7.

Additionally, we heat benzyl alcohol without $Cu(acac)_2$ at 140 and 170 °C, respectively, and in both cases with FTIR we exclusively detect benzaldehyde as shown in Fig. 5 (gray curves). It is the product of the oxidation of benzyl alcohol according to the reaction shown in Scheme 1.[54] The amounts of dibenzyl ether and benzyl benzoate detected by GC-MS are obviously below the detection limit of FTIR.

Now we discuss the quantities of the two compounds benzyl acetate and benzaldehyde we measured in comparison to what would be expected from the proposed chemical reactions. The chemical reactions themselves will be further discussed in section (d).

We assume that benzyl acetate is formed by the reaction of the acetylacetonate ligand with benzyl alcohol, as shown in Scheme 2.

Benzaldehyde is the oxidation product of benzyl alcohol as a result of the reduction of Cu^{2+} to Cu^{+} and finally Cu^{0} according to Scheme 3.

Having these reactions in mind and just considering the organic species detected, we can formulate an overall chemical reaction for the formation of Cu_2O, as shown in Scheme 4, and for Cu^{0} as displayed in Scheme 5.

From Scheme 4 it is evident that the formation of 1 mmol Cu_2O produces 4 mmol of benzyl acetate and 1 mmol of benzaldehyde. The initial concentration of $Cu(acac)_2$ in benzyl alcohol is 0.070 M, which means that 0.175 M benzyl alcohol (BnOH) are required, resulting in 0.140 M benzyl acetate, 0.035 M benzaldehyde and 0.070 M Cu^{+} (or 0.035 M Cu_2O) as summarized in eqn (2):

$$0.070\ \text{M}\ Cu^{2+} + 0.175\ \text{M BnOH} \rightarrow 0.140\ \text{M BnAc} + 0.035\ \text{M BnAd} + 0.070\ \text{M}\ Cu^{+} \quad (2)$$

According to Scheme 5, the formation of Cu at 170 °C follows eqn (3):

$$0.070\ \text{M}\ Cu^{2+} + 0.210\ \text{M BnOH} \rightarrow 0.140\ \text{M BnAc} + 0.070\ \text{BnAd} + 0.070\ \text{M}\ Cu^{0} \quad (3)$$

For the reaction at 140 °C, the measured concentration of benzyl acetate matches with the nominal value of 0.137 M within the resolution limit of our method, as shown in Fig. 5a and Table 1. At the same time, the sum of the concentrations of benzaldehyde in the control experiment (0.052 M) and the nominal value based on eqn (2) equals to 0.087 M, which is much lower than the actually measured concentration of just 0.115 M. Evidently, the Cu_2O nanoparticles are able to catalyze the oxidation of benzyl alcohol[58,59] to increase the benzaldehyde concentration beyond the expected value. The high coverage of the surface of the Cu_2O nanoparticles as mentioned before terminates the reaction at this

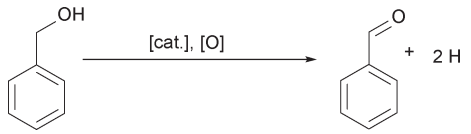

Scheme 1 Oxidation of benzyl alcohol to benzaldehyde.[54–57]

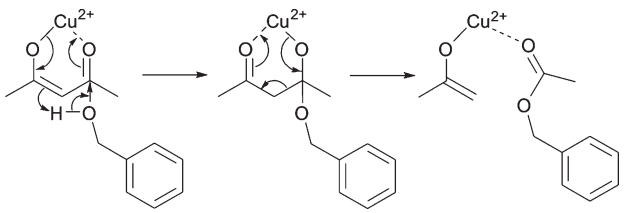

Scheme 2 Formation of benzyl acetate by nucleophilic attack of benzyl alcohol on one of the carbonyl groups of the acetylacetonate ligand.

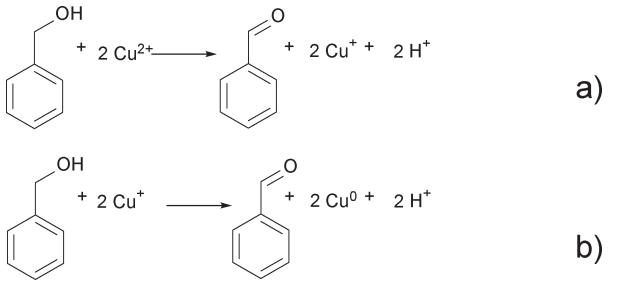

Scheme 3 Oxidation of benzyl alcohol to benzaldehyde and reduction of Cu^{2+} to Cu^{+} (a) and Cu^{+} to Cu^{0} (b).

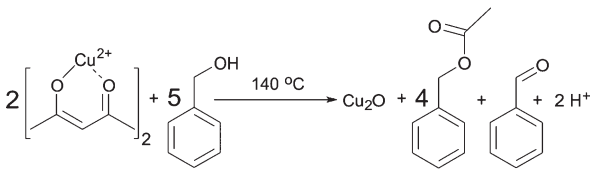

Scheme 4 Formation of Cu_2O, benzyl acetate and benzaldehyde from $Cu(acac)_2$ and benzyl alcohol at 140 °C.

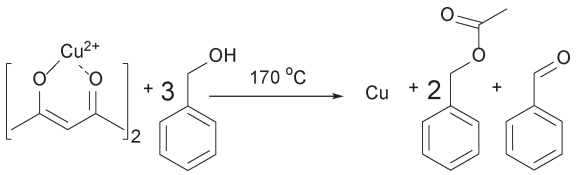

Scheme 5 Formation of Cu, benzyl acetate and benzaldehyde from $Cu(acac)_2$ and benzyl alcohol at 170 °C.

Table 1 Quantitative analysis of compounds formed during synthesis

		Synthesis at 140 °C		Synthesis at 170 °C	
Compound	Lower detection limit (M)	Expected value (M)	Measured value (M)	Expected value (M)	Measured value (M)
Benzyl acetate	0.007	0.140	0.137	0.140	0.112
Benzaldehyde	0.003	0.035	0.115	0.070	0.133
Dibenzyl ether	0.008	0	0	0	0.047
Control experiment		140 °C		170 °C	
Benzaldehyde	0.008	—	0.052	—	0.062

point without further reduction and we observe a saturation of the benzaldehyde concentration as evidenced in Fig. 5a.

For the reaction at 170 °C, based on the shape of the concentration profile of the organic compounds, the mechanism seems to be even more complex as shown in Fig. 5b. The final concentration of benzyl acetate equals to 0.112 M, which is lower than the nominal value of 0.140 M expected from eqn (3). This can be explained by the observation of acetone and acetylacetonate in the GC-MS chromatogram. Therefore, we assume that ligand exchange reactions, as shown in Scheme 6, are competing for $Cu(acac)_2$ with the reaction shown in Scheme 2.

In contrast to the synthesis at 140 °C, at 170 °C the measured concentration of benzaldehyde of 0.133 M agrees well with the expected value of 0.132 M, which is the sum of benzaldehyde from the control experiment (0.062 M) and from the reaction shown in eqn (3). This result is not surprising, because with the transformation of Cu_2O to Cu also the catalytically active nanoparticles disappear. However, in the very short time frame between 120–150 min we observed a rapid increase of the concentration of benzaldehyde and a decrease of the precursor concentration. It is interesting to note that only at this point of the reaction, the concentration of benzaldehyde does not correlate with the concentration of benzyl acetate, which indicates that the reactions shown in Scheme 6 might become more pronounced.

(d) Overview on chemical reactions taking place in solution during synthesis of copper nanoparticles. After the quantitative discussion of the different chemical reactions, we will have now a closer look at the reaction mechanisms. Benzyl acetate is exclusively forming due to the reaction between benzyl alcohol and acetylacetonate ligand as shown in Scheme 2 and as already reported for $Fe(acac)_3$,[15] $In(acac)_3$ [60] or $Zn(acac)_2$.[9] This step starts with the nucleophilic attack of the hydroxyl group of benzyl alcohol on one of the carbonyl groups of the acetylacetonate ligand. As a result, benzyl acetate and an enolate ligand form (Scheme 2). In the next step, benzyl alcohol coordinates to the copper ion. While the benzyl alcohol gets oxidized to benzaldehyde, Cu^{2+} is reduced to Cu^{+} as shown in Scheme 3a.

Up to here, we did not discuss, where the oxygen for the formation of the copper oxide comes from. Based on the results described above, we did not find any organic compounds that are typically ascribed to condensation reactions responsible for the formation of a metal–oxygen–metal bond.[15] Since the synthesis is performed under ambient conditions, we assume that water impurities in solvent can influence the formation of nanoparticles. In addition hydrogen ion formed during benzyl alcohol oxidation might react with oxygen to form water as proposed in Scheme 7a.[57,61,62] Once water is present, two possible scenarios for the formation of a Cu–O bond are possible. A water molecule directly coordinates to the enolate ligand, which leads to the formation of acetone and Cu(I)–OH species as shown in Scheme 7b. Alternatively, a benzyl alcohol molecules reacts with the enolate ligand, which leads to the formation of acetone and a copper benzyl alcoholate. These scenarios are both plausible, because traces of acetone were detected by GC-MS. A consecutive reaction of the copper alkoxide with water leads to a

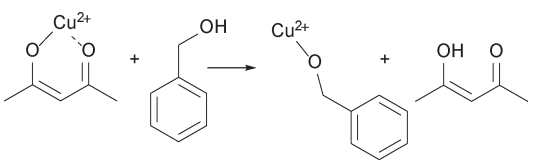

Scheme 6 Ligand exchange between acetylacetonate and benzyl alcohol as competition reaction.

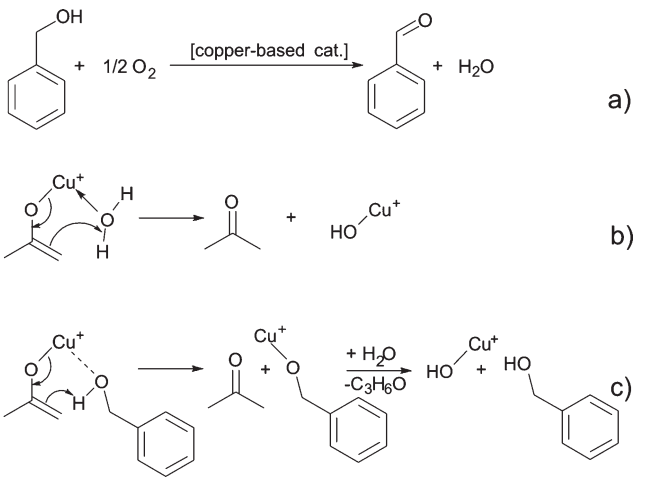

Scheme 7 (a) Formation of water, (b) reaction of the copper enolate with water to acetone and copper hydroxide, and (c) reaction of the copper enolate with benzyl alcohol to acetone and copper benzyl alcoholate, which further reacts to copper(I) hydroxide and benzyl alcohol.

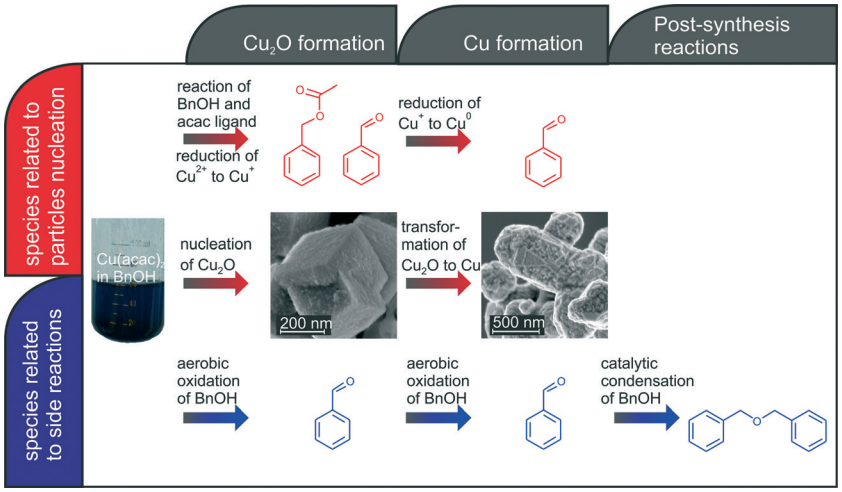

Fig. 6 Overview on organic and inorganic reactions taking place during synthesis of copper-based nanoparticles.

Cu(I)–OH species, as displayed in Scheme 7c. Finally, the Cu(I)–OH species condense with each other under release of water molecules and formation of Cu–O–Cu bonds.

4. Conclusions

Our *in situ* XAS/UV-vis/FTIR experiments reveal the dependence between the reactions leading to nucleation and growth of Cu-based nanoparticles and catalytic activity of newly forming nanoparticles as shown in Fig. 6. The organic species formed directly due to reduction of copper(II) acetylacetonate and nucleation of Cu_2O and Cu nanoparticles are shown in red. The nucleation of copper(I) oxide nanocubes co-occurs with the formation of benzyl acetate and benzaldehyde. Cu_2O subsequently transforms by solid-state reduction to metallic copper, which is accompanied by oxidation of benzyl alcohol to benzaldehyde. The parallel side reactions are shown in blue. We observe aerobic oxidation of benzyl alcohol to benzaldehyde. Overall, we can quantitatively differentiate between benzaldehyde forming in three independent reactions. Moreover, newly formed Cu nanoparticles show significant catalytic activity towards condensation of benzyl alcohol to dibenzylether. In this work, we demonstrate how to disentangle contributions of main and side reactions forming organic species during nanoparticle synthesis. That is particularly important when the nucleation of nanoparticles is coupled with the changes of the oxidation state of a metal.

Acknowledgements

We acknowledge the Swiss National Science Foundation (200021_137637) for the financial support and SNX Council of SNBL, ESRF for the beam time allocation. We thank the Scientific Center for Optical and Electron Microscopy (ScopeM) of ETH Zurich for the use of the SEM. We thank G. Grassi and F. Arc (Laboratory of Physical Chemistry, ETH Zurich) for the assistance with GC-MS measurements. MS thanks Dr. I. Bilecka and Dr. F. Heiligtag for their help in the initial phase of the project.

References

1 M. Niederberger, M. H. Bartl and G. D. Stucky, *J. Am. Chem. Soc.*, 2002, **124**, 13642–13643.
2 C. J. Dalmaschio, E. G. D. Firmiano, A. N. Pinheiro, D. G. Sobrinho, A. F. de Moura and E. R. Leite, *Nanoscale*, 2013, **5**, 5602–5610.
3 P. H. Mutin and A. Vioux, *J. Mater. Chem. A*, 2013, **1**, 11504–11512.
4 A. Vioux, *Chem. Mater.*, 1997, **9**, 2292–2299.
5 N. Pinna and M. Niederberger, *Angew. Chem., Int. Ed*, 2008, **47**, 5292–5304.
6 N. Shi, W. Cheng, H. Zhou, T. X. Fan and M. Niederberger, *Chem. Commun.*, 2015, **51**, 1338–1340.
7 G. Garnweitner and C. Grote, *Phys. Chem. Chem. Phys.*, 2009, **11**, 3767–3774.
8 I. M. Grabs, C. Bradtmoller, D. Menzel and G. Garnweitner, *Cryst. Growth Des.*, 2012, **12**, 1469–1475.
9 B. Ludi, M. J. Suess, I. A. Werner and M. Niederberger, *Nanoscale*, 2012, **4**, 1982–1995.
10 B. Ludi and M. Niederberger, *Dalton Trans.*, 2013, **42**, 12554–12568.
11 I. Bilecka, P. Elser and M. Niederberger, *ACS Nano*, 2009, **3**, 467–477.
12 G. Garnweitner and M. Niederberger, *J. Mater. Chem.*, 2008, **18**, 1171–1182.
13 K. B. Ramos, G. Clavel, C. Marichy, W. Cabrera, N. Pinna and Y. J. Chabal, *Chem. Mater.*, 2013, **25**, 1706–1712.
14 P. H. Mutin and A. Vioux, *Chem. Mater.*, 2009, **21**, 582–596.
15 M. Niederberger and G. Garnweitner, *Chem. – Eur. J.*, 2006, **12**, 7282–7302.
16 N. Pinna, M. Karmaoui and M. G. Willinger, *J. Sol-Gel Sci. Technol.*, 2011, **57**, 323–329.
17 M. Staniuk, M. Niederberger and D. Koziej, Nanoengineering: Fabrication, Properties, Optics, and Devices Xi, 2014, 9170.

18 M. Staniuk, O. Hirsch, N. Kranzlin, R. Bohlen, W. van Beek, P. M. Abdala and D. Koziej, *Chem. Mater.*, 2014, **26**, 2086–2094.
19 D. Koziej, M. D. Rossell, B. Ludi, A. Hintennach, P. Novak, J. D. Grunwaldt and M. Niederberger, *Small*, 2011, **7**, 377–387.
20 I. Olliges-Stadler, M. D. Rossell and M. Niederberger, *Small*, 2010, **6**, 960–966.
21 F. B. F. Silva, E. C. Paris, G. M. da Costa and C. Ribeiro, *RSC Adv.*, 2014, **4**, 53265–53272.
22 I. Bilecka, A. Hintennach, I. Djerdj, P. Novak and M. Niederberger, *J. Mater. Chem.*, 2009, **19**, 5125–5128.
23 B. Ludi, I. Olliges-Stadler, M. D. Rossell and M. Niederberger, *Chem. Commun.*, 2011, **47**, 5280–5282.
24 D. Koziej, F. Krumeich, R. Nesper and M. Niederberger, *J. Mater. Chem.*, 2009, **19**, 5122–5124.
25 N. Kranzlin, S. Ellenbroek, D. Duran-Martin and M. Niederberger, *Angew. Chem., Int. Ed.*, 2012, **51**, 4743–4746.
26 K. M. O. Jensen, C. Tyrsted, M. Bremholm and B. B. Iversen, *ChemSusChem*, 2014, **7**, 1594–1611.
27 G. Philippot, K. M. O. Jensen, M. Christensen, C. Elissalde, M. Maglione, B. B. Iversen and C. Aymonier, *J. Supercrit. Fluids*, 2014, **87**, 111–117.
28 H. Jensen, M. Bremholm, R. P. Nielsen, K. D. Joensen, J. S. Pedersen, H. Birkedal, Y. S. Chen, J. Almer, E. G. Sogaard, S. B. Iversen and B. B. Iversen, *Angew. Chem., Int. Ed.*, 2007, **46**, 1113–1116.
29 A. Michailovski, J. D. Grunwaldt, A. Baiker, R. Kiebach, W. Bensch and G. R. Patzke, *Angew. Chem., Int. Ed.*, 2005, **44**, 5643–5647.
30 Y. Zhou, Y. H. Lin and G. R. Patzke, *Prog. Chem.*, 2012, **24**, 1583–1591.
31 Y. Zhou, N. Pienack, W. Bensch and G. R. Patzke, *Small*, 2009, **5**, 1978–1983.
32 I. Olliges-Stadler, J. Stotzel, D. Koziej, M. D. Rossell, J. D. Grunwaldt, M. Nachtegaal, R. Frahm and M. Niederberger, *Chem. – Eur. J.*, 2012, **18**, 2305–2312.
33 I. Olliges-Stadler, M. D. Rossell, M. J. Suess, B. Ludi, O. Bunk, J. S. Pedersen, H. Birkedal and M. Niederberger, *Nanoscale*, 2013, **5**, 8517–8525.
34 Y. G. Sun, *Mater. Today*, 2012, **15**, 140–147.
35 J. Szlachetko, J. Sa, M. Nachtegaal, U. Hartfelder, J. C. Dousse, J. Hoszowska, D. L. A. Fernandes, H. Q. Shi and C. Stampfl, *J. Phys. Chem. Lett.*, 2014, **5**, 80–84.
36 M. Wuithschick, B. Paul, R. Bienert, A. Sarfraz, U. Vainio, M. Sztucki, R. Kraehnert, P. Strasser, K. Rademann, F. Emmerling and J. Polte, *Chem. Mater.*, 2013, **25**, 4679–4689.
37 J. Jaumot, R. Gargallo, A. de Juan and R. Tauler, *Chemom. Intell. Lab. Syst.*, 2005, **76**, 101–110.
38 W. H. Cassinelli, L. Martins, A. R. Passos, S. H. Pulcinelli, C. V. Santilli, A. Rochet and V. Briois, *Catal. Today*, 2014, **229**, 114–122.
39 Q. Tang, P. E. Carrington, Y. C. Horng, M. J. Maroney, S. W. Ragsdale and D. F. Bocian, *J. Am. Chem. Soc.*, 2002, **124**, 13242–13256.
40 C. A. Nunes, E. C. Resende, I. R. Guimaraes, A. S. Anastacio and M. C. Guerreiro, *Appl. Spectrosc.*, 2011, **65**, 692–697.
41 H. W. P. Carvalho, S. H. Pulcinelli, C. V. Santilli, F. Leroux, F. Meneau and V. Briois, *Chem. Mater.*, 2013, **25**, 2855–2867.
42 C. Marquez-Alvarez, I. Rodriguez-Ramos, A. Guerrero-Ruiz, G. L. Haller and M. Fernandez-Garcia, *J. Am. Chem. Soc.*, 1997, **119**, 2905–2914.
43 P. Conti, S. Zamponi, M. Giorgetti, M. Berrettoni and W. H. Smyrl, *Anal. Chem.*, 2010, **82**, 3629–3635.
44 O. Hirsch, G. B. Zeng, L. Luo, M. Staniuk, P. M. Abdala, W. van Beek, F. Rechberger, M. J. Suess, M. Niederberger and D. Koziej, *Chem. Mater.*, 2014, **26**, 4505–4513.
45 N. Kranzlin, M. Staniuk, F. J. Heiligtag, L. Luo, H. Emerich, W. van Beek, M. Niederberger and D. Koziej, *Nanoscale*, 2014, **6**, 14716–14723.
46 N. Kranzlin, W. van Beek, M. Niederberger and D. Koziej, *Adv. Mater. Interfaces*, 2015, DOI: 10.1002/admi.201500094.
47 B. Ravel and M. Newville, *J. Synchrotron Radiat.*, 2005, **12**, 537–541.
48 A. de Juan and R. Tauler, *Crit. Rev. Anal. Chem.*, 2006, **36**, 163–176.
49 A. Gaur, B. D. Shrivastava, K. Srivastava, J. Prasad and V. S. Raghuwanshi, *J. Chem. Phys.*, 2013, **139**, 034303.
50 S. Vukojevic, O. Trapp, J. D. Grunwaldt, C. Kiener and F. Schuth, *Angew. Chem., Int. Ed.*, 2005, **44**, 7978–7981.
51 D. E. Doronkin, M. Casapu, T. Gunter, O. Muller, R. Frahm and J. D. Grunwaldt, *J. Phys. Chem. C*, 2014, **118**, 10204–10212.
52 S. Gross and M. Bauer, *Adv. Funct. Mater.*, 2010, **20**, 4026–4047.
53 V. Guillerm, S. Gross, C. Serre, T. Devic, M. Bauer and G. Ferey, *Chem. Commun.*, 2010, **46**, 767–769.
54 Q. Zhang, W. Deng and Y. Wang, *Chem. Commun.*, 2011, **47**, 9275–9292.
55 T. Mallat and A. Baiker, *Chem. Rev.*, 2004, **104**, 3037–3058.
56 Z. C. Li, C. H. Chen, E. S. Zhan, N. Ta, Y. Li and W. J. Shen, *Chem. Commun.*, 2014, **50**, 4469–4471.
57 C. Keresszegi, D. Ferri, T. Mallat and A. Baiker, *J. Phys. Chem. B*, 2005, **109**, 958–967.
58 J. Fan, Y. Dai, Y. Li, N. Zheng, J. Guo, X. Yan and G. D. Stucky, *J. Am. Chem. Soc.*, 2009, **131**, 15568–15569.
59 G. Zhao, H. Hu, M. Deng, M. Ling and Y. Lu, *Green Chem.*, 2011, **13**, 55–58.
60 L. Zhang, G. Garnweitner, I. Djerdj, M. Antonietti and M. Niederberger, *Chem. – Asian J.*, 2008, **3**, 746–752.
61 Y. Xie, Z. F. Zhang, S. Q. Hu, J. L. Song, W. J. Li and B. X. Han, *Green Chem.*, 2008, **10**, 278–282.
62 M. Caravati, J. D. Grunwaldt and A. Baiker, *Phys. Chem. Chem. Phys.*, 2005, **7**, 278–285.